Optics Letters

Tuning Smith–Purcell radiation by rotating a metallic nanodisk array

Fei Chen,[1,†] Ren-Hao Fan,[1,†] Jun-Xuan Chen,[1] Yu Liu,[1] Ben-Qi Hou,[1] Ru-Wen Peng,[1,3] and Mu Wang[1,2,4]

[1]National Laboratory of Solid State Microstructures, School of Physics, and Collaborative Innovation Center of Advanced Microstructures, Nanjing University, Nanjing 210093, China
[2]American Physical Society, Hauppauge, New York 11788, USA
[3]rwpeng@nju.edu.cn
[4]muwang@nju.edu.cn
[†]These authors contributed equally to this work.

Received 26 December 2022; revised 15 February 2023; accepted 2 March 2023; posted 3 March 2023; published 4 April 2023

Smith–Purcell radiation (SPR) refers to the far-field, strong, spike radiation generated by the interaction of the evanescent Coulomb field of the moving charged particles and the surrounding medium. In applying SPR for particle detection and nanoscale on-chip light sources, wavelength tunability is desired. Here we report on tunable SPR achieved by moving an electron beam parallel to a two-dimensional (2D) metallic nanodisk array. By in-plane rotating the nanodisk array, the emission spectrum of the SPR splits into two peaks, with the shorter-wavelength peak blueshifted and the longer-wavelength one redshifted by increasing the tuning angle. This effect originates from the fact that the electrons fly effectively over a one-dimensional (1D) quasicrystal projected from the surrounding 2D lattice, and the wavelength of SPR is modulated by quasiperiodic characteristic lengths. The experimental data are in agreement with the simulated ones. We suggest that this tunable radiation provides free-electron-driven tunable multiple photon sources at the nanoscale. © 2023 Optica Publishing Group

https://doi.org/10.1364/OL.484324

Smith–Purcell radiation (SPR) [1–4] refers to the far-field radiation induced by the interaction between the evanescent Coulomb field of moving charged particles and the surrounding medium, typically with periodic structures. This interaction could lead to a strong spike SPR at a resonant frequency of the periodic structures, which shows great potential applications in nanoscale light sources. The frequencies of the SPR may vary from x rays [5], ultraviolet [6], visible [7,8], infrared (IR) [9–11], to terahertz ranges [10–13]. It is widely used in particle detection [14], nanoscale on-chip light sources [15], and particle accelerators [16,17]. In those applications, tunable SPR is desired to improve the performance of the source in radiation polychromaticity and power density.

To achieve a tunable SPR, one may tailor the interaction between charged particles and the surrounding medium by artificially designing the nanostructures of the materials to regulate the electromagnetic and optical properties. Over the past decades, metasurfaces [18–20], photonic crystals [21,22], and graphene [23,24] have been effectively combined to tune the frequency, amplitude, and propagation direction of SPR. For example, the polarization of the generated radiation on the surface of Babinet metasurfaces can be controlled through induced cross-coupled electric and magnetic dipoles, showing advanced properties to that on the surface of gratings [18,25]. To further tailor the diffraction of SPR, the emerging non-periodic nanostructures with strong short-range disorder are also introduced to generate SPR with surprising robustness [26,27]. In general, the reciprocal lattice vector of the periodic lattice interacting with electrons determines the frequency and radiation angle of the SPR. When the structure loses its periodicity, strong radiation characteristics may still be generated since the aperiodic arrays may possess momentum with certain preferential wave vectors corresponding to the characteristic lengths [28]. By calculating the radiation distribution of a one-dimensional (1D) quasiperiodic Fibonacci particle array, the emission angles and frequency distributions of quasiperiodic structures are still found to exhibit strong features owing to their typical characteristic lengths [28]. Besides, the 1D quasiperiodic array can be obtained simply by projecting a two-dimensional (2D) lattice in a direction with an irrational slope [29–33]. Moving the electron beam arbitrarily oriented in a plane parallel to the surface of an anisotropic particle array is also proposed and theoretically considered [34]. Up to now, a method to easily and flexibly tune SPR, especially in a dynamically tunable manner, remains challenging in the experiment so far.

In this work, we experimentally demonstrate tunable SPR when the electron beam flies along different directions over a surface of a 2D gold nanodisk array. The moving electrons interact effectively with a tunable 1D quasiperiodic chain, which is the projection from the 2D lattice into the electron beam trajectory. The multiple characteristic lengths of the quasiperiodic chains lead to different radiative responses. It follows that the SPR can be continuously regulated to produce tunable far-field radiation patterns in characteristic modes.

A schematic diagram of this tunable SPR is shown in Fig. 1(a). A 2D gold nanodisk array is fabricated on the silicon substrate. The nanodisks are arranged in a square lattice. The radiation is generated when the electron beam is applied along the x'

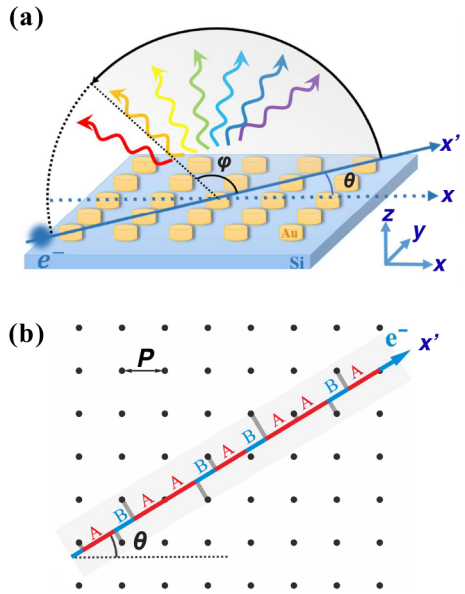

Fig. 1. (a) Schematic showing the electron beam moving along the x' direction parallel to the surface of a 2D gold nanodisk array on a silicon substrate. The angle between the x and x' axis is θ, and the radiation angle is φ in the x'–z plane. (b) Schematic of the effective quasiperiodic chains when the electron beam flies along the x' direction.

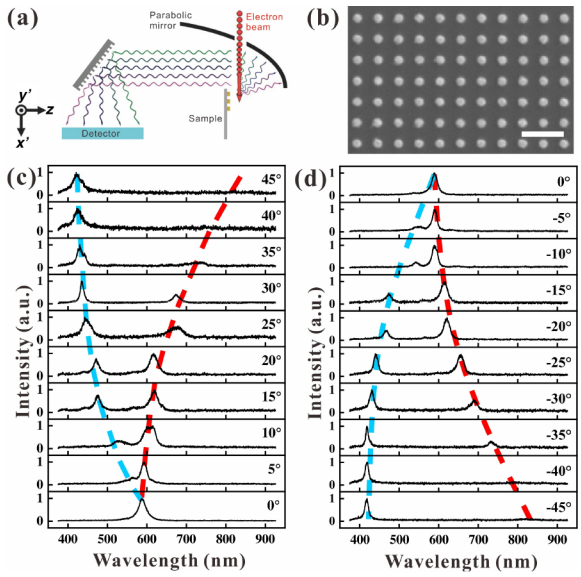

Fig. 2. (a) Schematic of the SPR measuring system. (b) SEM micrograph of the gold nanodisk sample. The scale bar is 300 nm. (c) Spectra collected by increasing the rotation angle from 0° to 45°. (d) Spectra collected by increasing the rotation angle from –45° to 0°. The blue and red dashed curves represent the blueshift and redshift of the peaks, respectively.

direction parallel to the surface of this 2D nanodisk array. We define the rotation angle θ as the angle between the moving direction of the electron beam and the x axis in the x–y plane and the radiation angle φ as the angle between the radiation direction and the electron trajectory in the x'–z plane.

Usually, the electromagnetic field around the moving charged particle is confined around the particle in the form of exponential decay and belongs to the evanescent field, and electric dipoles are induced through the evanescent Coulomb field. A beam of flying charged particles (electrons in this work) passes in parallel across the periodic structure, and the evanescent field around the electrons in turn interacts with the structures underneath, thereby exciting the electric dipole oscillations in the lattice. Meanwhile, the electromagnetic energy originally confined in the evanescent field around the electrons can be radiated to the far field following the principle of diffraction and wave vector compensation from the periodic structure. The relation between the radiation wavelength and the electron velocity can be described as [1]

$$\lambda = \frac{s}{m}\left(\frac{c}{v} - \cos\varphi\right), \tag{1}$$

where s is the periodicity of the periodic structure, m is the diffraction order, c is the speed of light, v is the speed of the electrons, and φ is the angle between the electron flight direction and the radiation propagation direction. This relationship is the key to study the Smith–Purcell effect.

1D quasiperiodic lattices can be obtained along the electron trajectory by mechanically rotating this 2D nanodisk array [29–33], and Fig. 1(b) shows a schematic diagram of this transformation. For the convenience of calculation, we simplify the gold nanodisks into a 2D periodic lattice. When the electron beam moves at angle θ, the effectively influenced region of the Coulomb field of the electron beam is illustrated by the shadow in Fig. 1(b). The width of this region is of the order of the lattice parameter P in our experiment. By projecting the grid points within this range to the electron beam trajectory along the direction perpendicular to x', we obtain a sequence of length as shown in Fig. 1(b), which is arranged as ABAABABAABA... This quasiperiodic sequence contains two units A and B, where the characteristic scale of unit A is $l_A = P\cos\theta$, and the characteristic scale of unit B is $l_B = P\sin\theta$. Therefore, when the electron beam passes over the sample surface, it will sense and interact with the quasiperiodic structures underneath, leading to a strong resonance with two characteristic lengths of A and B.

It is noteworthy that, according to the self-similarity of the quasiperiodic sequence [29,33], there are some simple composite units repeated in the sequence with their sizes representing the characteristic lengths of this structure, such as $l_A + l_B$ and $2l_A$. Therefore, we can also receive radiative responses related to these repeated lengths. According to the wavelength-angle relationship of SPR, radiation wavelengths corresponding to the repeated lengths can be obtained as $\lambda_{1,m} = \frac{P\cos\theta}{m}\left(\frac{c}{v} - \cos\varphi\right)$, $\lambda_{2,m} = \frac{P\sin\theta}{m}\left(\frac{c}{v} - \cos\varphi\right)$, $\lambda_{3,m} = \frac{P(\cos\theta+\sin\theta)}{m}\left(\frac{c}{v} - \cos\varphi\right)$, etc., where m is the diffraction order. By changing the rotation angle θ, the characteristic lengths are adjusted accordingly. Only two modes $\lambda_{1,1} = P\cos\theta(c/v - \cos\varphi)$ and $\lambda_{3,1} = P(\cos\theta + \sin\theta)(c/v - \cos\varphi)$ can be detected in our experimental setup with the wavelengths within the range of 380–950 nm, and the lattice parameter P is 150 nm.

Experimentally, a 30 keV electron beam is launched in a field-emission scanning electron microscope (SEM, Zeiss ULTRA 55), moving parallel to the surface of the sample, as illustrated in Fig. 2(a). The sample is positioned at the focal point of the parabolic mirror to ensure maximum collection intensity. The distance between the focused electron beam and the surface of the sample is kept around 50 nm. The emitted photons are collected by the parabolic mirror. Via reflection of the parabolic

mirror, the radiated light is directed to a grating spectrometer associated with a charge-coupled device (CCD) camera [35–37]. From the system's setup, we may find that only the photons emitted upwards—i.e., the radiation angle φ is between 90° and 180°—can be collected by the parabolic mirror, as illustrated in Fig. 2(a). In experiments, the main radiation angle φ may also be affected by the collection efficiency of the parabolic mirror. We collect a spectrum in a wavelength range of 380–950 nm, and the integration time is set as 20.0 s.

The gold nanodisk array has been fabricated on the silicon substrate by electron beam lithography, followed by lift-off processing. The gold layer is 20 nm in thickness. For stronger adhesion, a layer of 2-nm thick titanium is homogeneously deposited on the silicon surface before gold deposition. The diameters of the nanodisks are 60 nm. The nanodisks are arranged orthogonally to form a square lattice with a periodicity of 150 nm. The SEM micrograph of the nanodisk array is shown in Fig. 2(b).

The experimentally detected spectra of the gold nanodisk array are shown in Fig. 2(c). We collect the spectra with θ changing from 0° to 45° in 5° intervals by rotating the sample in the x'–y' plane. When the rotation angle equals 0°, the spectrum has only one peak around 580 nm. The spread of the peaks in the spectrum is due to the fact that the signal is collected with a radiation angle φ between 90° and 180°. By increasing θ from 0° to 45° in the x'–y' plane, the peak splits into two. The shorter-wavelength peak blueshifts, whereas the longer-wavelength peak redshifts. When the rotation angle reaches 45°, only one peak around 420 nm survives in the spectrum. We also collect the spectra with the rotation angle θ from –45° to 0° in 5° intervals, as shown in Fig. 2(d). One may find the splitting of the peaks reverses itself. Two peaks recombine into one due to the quartic symmetry in the nanodisk array.

The blue dashed line in Fig. 2(c) represents the blueshift of the peak position with the increase of the rotation angle, which is the radiation mode $\lambda_{1,1}$ associated with the characteristic length $P\cos\theta$. We fix the radiation angle $\varphi = 145°$, which locates around the center of the detected range of φ between 90° and 180°, to estimate the theoretically predicted modes. As the angle θ increases, the characteristic length $P\cos\theta$ decreases. The red dashed line represents the redshift of the peak, which is the radiation mode $\lambda_{3,1}$ associated with the characteristic length $P(\cos\theta+\sin\theta)$, and the characteristic length $P(\cos\theta+\sin\theta)$ increases as the angle θ increases. In the detectable range of our experiment, we observed that the two kinds of radiation modes $\lambda_{1,1}$ and $\lambda_{3,1}$ corresponding to the two characteristic lengths possess blueshift and redshift features, respectively, with the change of the rotation angle. It is proved that by rotating the sample, which is equivalent to change the moving direction of the electron beam, we can obtain quasiperiodic chains with different characteristic lengths, leading to continuously tunable SPR with multiple modes.

To further analyze this tunable SPR, we calculated the electric field radiated from this sample using a commercial software (COMSOL Multiphysics). We obtained the far-field radiation intensity distribution in the wavelength range 400–850 nm under electron velocity $v = 0.329c$.

According to the wavelength-angle relationship of SPR, multiple radiation wavelengths corresponding to the characteristic lengths can be obtained. Figures 3(a)–3(d) show the far-field radiation intensity map on the wavelength and the radiation angle φ when the rotation angle θ equals 0°, 15°, 30°, and 45°, respectively. To show the correspondence between the simulation results and the experimentally collected spectra, we integrate the computed wavelength-angle distributions over the selected areas indicated by the yellow dashed boxes in Fig. 3 to reconstruct the spectra. By changing the rotation angle θ, as shown in Fig. 3, we can find that the wavelength and the radiation angle φ of SPR are modulated correspondingly. We can identify a mode around 560 nm at $\theta = 0°$, corresponding to the measured spectrum just below 600 nm [Fig. 3(a)]. This peak splits into two modes when $\theta = 15°$ [Fig. 3(b)]. When $\theta = 30°$, one mode redshifts and the other blueshifts [Fig. 3(c)], which is similar to the experimentally measured modes $\lambda_{1,1}$ and $\lambda_{3,1}$. When the rotation angle θ increases to 45°, we find only a peak around 420 nm remains [Fig. 3(d)], which is consistent with the experiments.

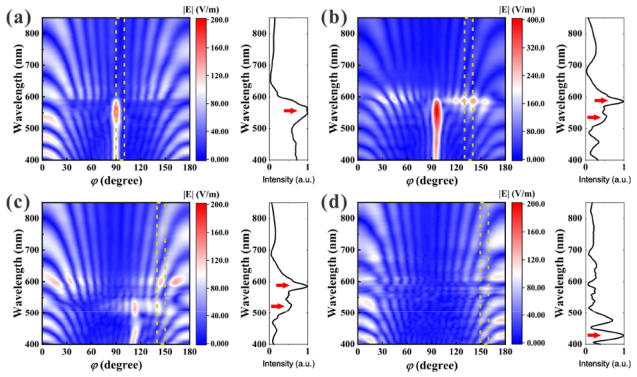

Fig. 3. Far-field radiation intensity mapping on the wavelength and the radiation angle φ with different rotation angles: (a) $\theta = 0°$; (b) $\theta = 15°$; (c) $\theta = 30°$; and (d) $\theta = 45°$. The curve on the right side represents the integrated intensity of electric field $|\mathbf{E}|$ over the selected area marked by yellow dashed boxes. The red arrows highlight the peaks corresponding to the experimentally collected ones.

The model proposed here regarding the radiated wavelength, rotation angle, and radiated angle is simplified. Some other factors, such as the size of nanodisks, the separation of the electron beam and sample surface, etc., have been ignored. The radiation in 3D space becomes more complicated. Further exploration of 3D far-field radiation patterns is essential. We calculate the radiation distribution in four configurations and obtain different radiation patterns shown in Fig. 4. The calculated far-field radiation pattern when $\theta = 0°$ and $\lambda = 580$ nm is shown in Fig. 4(a). The main radiation angle φ is around 90°, which is consistent with Fig. 3(a). The calculated far-field radiation patterns when $\theta = 30°$, $\lambda = 450$ nm; $\theta = 30°$, $\lambda = 680$ nm; and $\theta = 45°$, $\lambda = 420$ nm are shown in Figs. 4(b)–4(d), respectively. The corresponding main radiation angle φ is around 125°, 125°, and 155°, respectively. From the calculated radiation angle φ in far-field radiation patterns, we can derive the characteristic lengths in the structure based on Eq. (1) to verify the rationality of our model. The characteristic lengths of the structure can be deduced according to Eq. (1) as 125 nm, 188 nm, and 106 nm, respectively, which is consistent with the characteristic lengths as $P\cos30° = 130$ nm, $P(\cos30°+\sin30°) = 205$ nm and $P\cos45° = 106$ nm when the period of the sample is $P = 150$ nm.

This work demonstrates that a mechanically rotatable 2D nanodisk array can generate tunable SPR with the electron beam moving along different directions. The effective lattices along

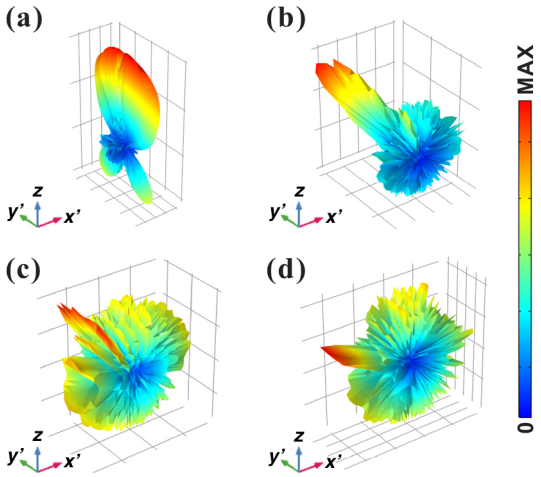

Fig. 4. Simulated 3D far-field radiation patterns for four situations: (a) $\theta = 0°$, $\lambda = 580$ nm; (b) $\theta = 30°$, $\lambda = 450$ nm; (c) $\theta = 30°$, $\lambda = 680$ nm; and (d) $\theta = 45°$, $\lambda = 420$ nm.

the moving direction of the electron beam can be treated as tunable 1D quasiperiodic chains. The quasiperiodic chains with characteristic wave vectors can be used to couple the bound energy from the evanescent wave generated by the electron beam to the far field due to wave vector compensation. By rotating the sample, the characteristic lengths of the quasiperiodic chains are tuned, resulting in tunable wave vectors in reciprocal space. Experimental results show that the wavelength of this SPR can be continuously modulated. This complex spatial distribution of radiated light may provide a promising approach for generating tunable multiple photon sources for nanoscale on-chip applications.

Funding. National Key R & D Program of China (2020YFA0211300, 2022YFA1404303); National Natural Science Foundation of China (12234010, 61975078, 11974177).

Disclosures. The authors declare no conflicts of interest.

Data availability. The data supporting the findings of this study are available from the corresponding authors upon reasonable request.

REFERENCES

1. S. J. Smith and E. M. Purcell, Phys. Rev. **92**, 1069 (1953).
2. Z. Su, B. Xiong, Y. Xu, Z. Cai, J. Yin, R. Peng, and Y. Liu, Adv. Opt. Mater. **7**, 1801666 (2019).
3. J. H. Brownell, J. Walsh, and G. Doucas, Phys. Rev. E **57**, 1075 (1998).
4. J. P. Bachheimer, Phys. Rev. B **6**, 2985 (1972).
5. M. J. Moran, Phys. Rev. Lett. **69**, 2523 (1992).
6. O. Haeberlé, P. Rullhusen, J.-M. Salomé, and N. Maene, Phys. Rev. E **49**, 3340 (1994).
7. G. Doucas, J. H. Mulvey, M. Omori, J. Walsh, and M. F. Kimmitt, Phys. Rev. Lett. **69**, 1761 (1992).
8. G. Kube, H. Backe, H. Euteneuer, A. Grendel, F. Hagenbuck, H. Hartmann, K. H. Kaiser, W. Lauth, H. Schöpe, G. Wagner, T. Walcher, and M. Kretzschmar, Phys. Rev. E **65**, 056501 (2002).
9. J. Urata, M. Goldstein, M. F. Kimmitt, A. Naumov, C. Platt, and J. E. Walsh, Phys. Rev. Lett. **80**, 516 (1998).
10. L. Liu, H. Chang, C. Zhang, Y. Song, and X. Hu, Phys. Rev. B **96**, 165435 (2017).
11. Y. Song, J. Du, N. Jiang, L. Liu, and X. Hu, Opt. Lett. **43**, 3858 (2018).
12. S. E. Korbly, A. S. Kesar, J. R. Sirigiri, and R. J. Temkin, Phys. Rev. Lett. **94**, 054803 (2005).
13. D. Y. Sergeeva, A. S. Aryshev, A. A. Tishchenko, K. E. Popov, N. Terunuma, and J. Urakawa, Opt. Lett. **46**, 544 (2021).
14. S. E. Korbly, A. S. Kesar, R. J. Temkin, and J. H. Brownell, Phys. Rev. ST Accel. Beams **9**, 022802 (2006).
15. C. Roques-Carmes, S. E. Kooi, Y. Yang, A. Massuda, P. D. Keathley, A. Zaidi, Y. Yang, J. D. Joannopoulos, K. K. Berggren, I. Kaminer, and M. Soljačić, Nat. Commun. **10**, 3176 (2019).
16. J. Breuer and P. Hommelhoff, Phys. Rev. Lett. **111**, 134803 (2013).
17. K. J. Leedle, R. F. Pease, R. L. Byer, and J. S. Harris, Optica **2**, 158 (2015).
18. Z. Wang, K. Yao, M. Chen, H. Chen, and Y. Liu, Phys. Rev. Lett. **117**, 157401 (2016).
19. Z. Yu, L. Zhang, W. Liu, J. Yin, Y. Liu, Q. Jia, B. Sun, H. Xu, and S. Liu, Phys. Rev. Appl. **17**, 014038 (2022).
20. T. Fu, D. Wang, Z. Yang, Z. Deng, and W. Liu, Opt. Express **29**, 26983 (2021).
21. S. Yamaguti, J. Inoue, O. Haeberlé, and K. Ohtaka, Phys. Rev. B **66**, 195202 (2002).
22. C. Luo, M. Ibanescu, S. G. Johnson, and J. D. Joannopoulos, Science **299**, 368 (2003).
23. L. Qi, M. Wu, and X. Han, Appl. Opt. **61**, 4773 (2022).
24. Z. Su, F. Cheng, L. Li, and Y. Liu, ACS Photonics **6**, 1947 (2019).
25. W. Liu, W. Li, Z. He, and Q. Jia, AIP Adv. **5**, 127135 (2015).
26. I. Kaminer, S. E. Kooi, R. Shiloh, B. Zhen, Y. Shen, J. J. López, R. Remez, S. A. Skirlo, Y. Yang, J. D. Joannopoulos, A. Arie, and M. Soljačić, Phys. Rev. X **7**, 011003 (2017).
27. Y. Yang, A. Massuda, C. Roques-Carmes, S. E. Kooi, T. Christensen, S. G. Johnson, J. D. Joannopoulos, O. D. Miller, I. Kaminer, and M. Soljačić, Nat. Phys. **14**, 894 (2018).
28. J. R. M. Saavedra, D. Castells-Graells, and F. Javier García de Abajo, Phys. Rev. B **94**, 035418 (2016).
29. R. K. P. Zia and W. J. Dallas, J. Phys. A: Math. Gen. **18**, L341 (1985).
30. R. Peng, A. Hu, S. Jiang, C. Zhang, and D. Feng, Phys. Rev. B **46**, 7816 (1992).
31. R. Peng, M. Wang, A. Hu, S. Jiang, G. Jin, and D. Feng, Phys. Rev. B **52**, 13310 (1995).
32. E. Abe, Y. Yan, and S. J. Pennycook, Nat. Mater. **3**, 759 (2004).
33. Y. K. Vekilov and M. A. Chernikov, Phys.-Usp. **53**, 537 (2010).
34. D. I. Garaev, D. Y. Sergeeva, and A. A. Tishchenko, Phys. Rev. B **103**, 075403 (2021).
35. Y. Hu, D. Zhao, Z. Wang, F. Chen, X. Xiong, R. Peng, and M. Wang, Opt. Lett. **42**, 1744 (2017).
36. Y. Hu, F. Chen, Y. Gao, X. Xiong, R. Peng, and M. Wang, Opt. Lett. **43**, 158 (2018).
37. T. Han, S. Zu, Z. Li, M. Jiang, X. Zhu, and Z. Fang, Nano Lett. **18**, 567 (2018).

210.28.141.20 on 2023-08-16 09:07:48